

RESEARCH LETTER

10.1029/2018GL078137

Special Section:

Cassini's Final Year: Science Highlights and Discoveries

Key Points:

- The high-frequency edge of a continuous whistler mode emission displayed a clear decrease in frequency near plus-minus 40 degrees latitude at altitudes of 1.1 to 1.3 R_s .
- Closer examination reveals that these dropouts are associated with abrupt electron density decreases occurring on field lines connected to the A and B rings.
- We conclude that magnetic field lines connected to the rings are evacuated of plasma relative to field lines just outside the A ring.

Supporting Information:

- Supporting Information S1

Correspondence to:

W. M. Farrell,
william.m.farrell@nasa.gov

Citation:

Farrell, W. M., Hadid, L. Z., Morooka, M. W., Kurth, W. S., Wahlund, J.-E., MacDowall, R. J., et al. (2018). Saturn's plasma density depletions along magnetic field lines connected to the main rings. *Geophysical Research Letters*, 45, 8104–8110. <https://doi.org/10.1029/2018GL078137>

Received 30 MAR 2018

Accepted 29 JUL 2018

Accepted article online 3 AUG 2018

Published online 22 AUG 2018

©2018. The Authors.

This is an open access article under the terms of the Creative Commons Attribution-NonCommercial-NoDerivs License, which permits use and distribution in any medium, provided the original work is properly cited, the use is non-commercial and no modifications or adaptations are made.

Saturn's Plasma Density Depletions Along Magnetic Field Lines Connected to the Main Rings

W. M. Farrell¹ , L. Z. Hadid² , M. W. Morooka² , W. S. Kurth³ , J.-E. Wahlund² , R. J. MacDowall¹, A. H. Sulaiman³ , A. M. Persoon³ , and D. A. Gurnett³ 

¹NASA Goddard Space Flight Center, Greenbelt, MD, USA, ²Swedish Institute of Space Physics, Uppsala, Sweden, ³Department of Physics and Astronomy, University of Iowa, Iowa City, IA, USA

Abstract We report on a set of clear and abrupt decreases in the high-frequency boundary of whistler mode emissions detected by Cassini at high latitudes (about $\pm 40^\circ$) during the low-altitude proximal flybys of Saturn. These abrupt decreases or dropouts have start and stop locations that correspond to L shells at the edges of the A and B rings. Langmuir probe measurements can confirm, in some cases, that the abrupt decrease in the high-frequency whistler mode boundary is associated with a corresponding abrupt electron density dropout over evacuated field lines connected to the A and B rings. Wideband data also reveal electron plasma oscillations and whistler mode cutoffs consistent with a low-density plasma in the region. The observation of the electron density dropout along ring-connecting field lines suggests that strong ambipolar forces are operating, drawing cold ionospheric ions outward to fill the flux tubes. There is an analog with the refilling of flux tubes in the terrestrial plasmasphere. We suggest that the ring-connected electron density dropouts observed between 1.1 and 1.3 R_s are connected to the low-density ring plasma cavity observed overtop the A and B rings during the 2004 Saturn orbital insertion pass.

Plain Language Summary We present Cassini observations during the close passes by the planet Saturn indicating that plasma on magnetic field lines that pass through the A and B rings is of anomalously low density. These observations are consistent with the Saturn orbit insertion observations of a plasma cavity located at equatorial regions overtop the dense B ring. Using a terrestrial analogy, we suggest that the low-density conditions overtop the rings create an electrical force, called an *ambipolar electric field* that draws plasma out of the ionosphere in an attempt to replenish the plasma void found at equatorial regions.

1. Introduction

The Cassini spacecraft came to a spectacular end on 15 September 2017 after plunging into the midlatitude atmosphere at a speed close to 34 km/s. During the preceding 6 months, the spacecraft executed a set of 22 Grand Finale/Proximal orbits taking the spacecraft periapsis to low altitudes between the equatorial D ring and planet. During these passes, the spacecraft transited magnetic field lines directly connected to the main rings, and the electron plasma properties at these locations were sensed by the Cassini Radio and Plasma Wave Science (RPWS) Langmuir probe (LP) and very low frequency plasma wave receiver system (Wahlund et al., 2018).

Figure 1 shows the trajectory of Cassini during one of these passes which is representative of the set. As indicated, the spacecraft directly intercepts the entire range of ring-connected magnetic field lines. The solar elevation angle during this period is large, at $+26.7^\circ$, with the Sun shining on the northward face of the rings. The A ring extends in radial distance from approximately 2.02 to 2.27 R_s , and the B ring extends from ~ 1.55 to 1.95 R_s (Connerney, 1986).

The only other time Cassini examined the plasma character on magnetic field lines connected to the rings was during the 2004 orbit insertion event (Saturn orbit insertion [SOI]; Gurnett et al., 2005; Young et al., 2005). During this overflight, the solar elevation angle was near -24° , with the Sun shining directly on the southern face of the rings. Cassini flew overtop the unlit northward face of the rings. Using known plasma wave signatures, the RPWS instrument detected the presence of a clear and distinct ring plasma cavity at an altitude of $< 24,000$ km over the main rings with densities as low as 0.04 electrons/cm³ near the center of the B ring at $L = 1.76$ (Farrell et al., 2017; Gurnett et al., 2005; Xin et al., 2006). The electron density at the outer edge of the A ring ($L = 2.27$) was close to 120 electrons/cm³ (Persoon et al., 2015) but abruptly

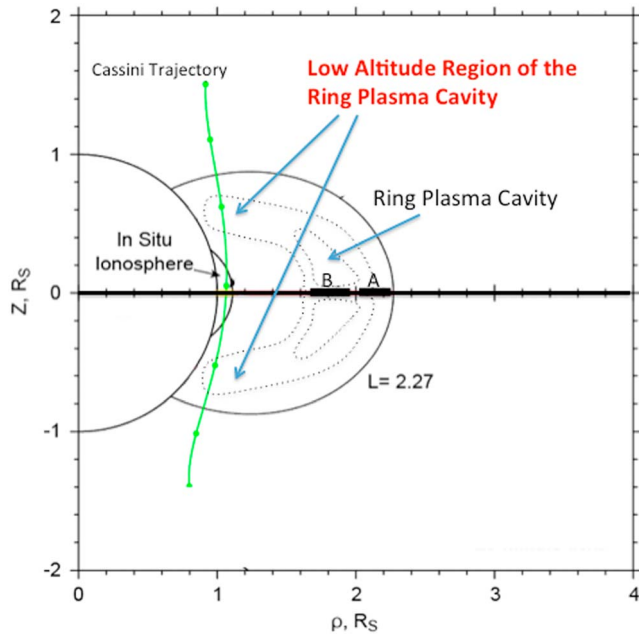


Figure 1. An example of the Cassini trajectory in cylindrical coordinates (green line) and an illustration of the ring plasma cavity. The Cassini trajectory transits magnetic field lines connected to the rings and the cavity. This pass is representative of the set of Grand Finale passes, where the spacecraft passed between the ionosphere and inner edge of the D ring. The A ring extends from 2.02 to 2.27 R_s , and the B ring extends from ~ 1.55 to $1.95 R_s$ (Connerney, 1986).

decreased over the plasma-absorbing rings by over a factor of 3,000 to $0.04/\text{cm}^3$ at $L = 1.76$. The ring plasma cavity is illustrated in Figure 1 as dotted lines representing density contours.

The observation of the low-density ring plasma cavity found over the A and B rings during SOI was unexpected. Voyager era modeling suggested that meteoric impacts would create an impact ionized plasma outflow with the greatest outflow over the densest portion of the rings (at the center of the B ring; Wilson & Waite Jr., 1989). These outflowing ions were expected to migrate along connecting field lines to then be deposited at Saturn's ionospheric exobase. It was anticipated that this ring-originating heavy ion inflow would then disrupt the ionospheric hydrogen chemistry (Connerney & Waite, 1984). The presence of the cavity found during SOI suggests that the ring plasma is not impact driven but driven instead possibly by photolytic processes as suggested by Tseng et al. (2010, 2013).

The proximal orbits created multiple occasions to examine the SOI-observed ring plasma cavity from magnetically connected locations closer to the field line footprint. We will present evidence that this ring plasma cavity over the main A and B rings extends along the connecting magnetic field lines to lower altitudes and thus was detected by the Cassini spacecraft during the proximal orbit period.

2. Methodology

Figure 2 shows a Cassini frequency-versus-time spectrogram during the periapsis period from proximal orbit 275. The observations are from the low rate survey data set with temporal resolution at a given frequency near 16 s (see Table 2 of Gurnett et al., 2004). Shown in the figure is the electron cyclotron frequency (labeled as f_{ce}) derived directly from the Cassini magnetometer observations (Dougherty et al., 2004). Below this line, near closest approach from about 02:50 to 03:30 spacecraft event time (SCET) is a broadband emission extending up to 100 kHz identified previously as a whistler mode signal (Wahlund et al., 2018). The high-frequency cutoff for this particular event is limited by the electron plasma frequency (labeled by f_{pe}), providing a direct indication of the electron density. These whistler mode-derived electron density values for this and other ionosphere passes have been compared directly with the RPWS LP measurements, and they effectively overlay each other (see, e.g., Figure 2 of Wahlund et al., 2018).

However, at higher latitudes in the north and south, between 02:35 to 02:45 SCET and later at 03:30 to 03:40 SCET, respectively, we find the presence of an anomalous *dropout* or frequency decrease in the high-frequency boundary of the whistler mode emission. The feature is identified as a clear and distinct decrease in this boundary from about 20 to below 6 kHz between 02:35 to 02:45 SCET and a similar feature occurring again later at 03:30 to 03:40 SCET. These abrupt dropouts that are observed both inbound and outbound are identified in the spectrogram.

If these dropouts in the whistler mode high-frequency edge are associated with changes in the electron density, these reductions would represent an abrupt factor of 10 density dropout from 5 to $0.4/\text{cm}^3$ along locations that magnetically map to the A and B ring systems between L of 1.5 to 2.3.

Many of the proximal orbits had these dropout features near $\pm 40^\circ$ along Cassini's path. In some cases, other emissions created in remote locations would mask or obscure these features (see Figures S8 and S9 in the

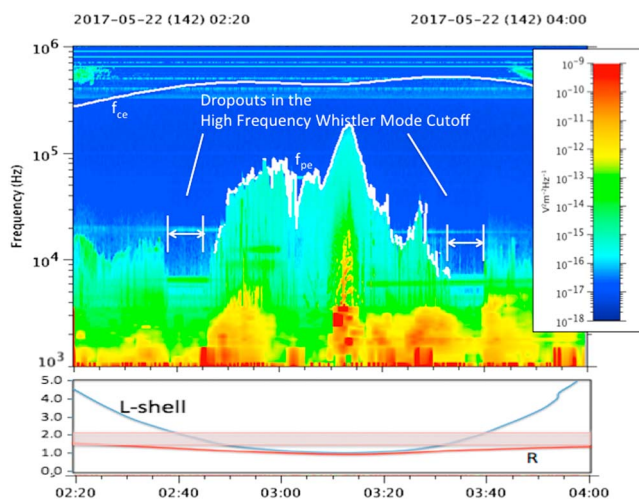


Figure 2. The Cassini Radio and Plasma Wave Science frequency versus time spectrogram from the proximal periapsis period of orbit 275. The broadband emission below 100 kHz is a whistler mode signal. The figure identifies the two dropouts in the high-frequency cutoff of the whistler mode emission occurring on L shell values between 1.5 and 2.2 (the shaded region in the bottom panel).

supporting information; Menietti et al., 2018). However, in the northern sunlit hemisphere, in 15 out of 22 proximal cases, the abrupt dropout feature was observed. The interpretation of the southern hemisphere passes is more complicated since an electron density dropout was also reported associated with the ring shadow at latitudes below $\sim 38^\circ\text{S}$ (Hadid et al., 2018; Wahlund et al., 2018). However, a dropout in the whistler mode high-frequency edge extending to latitudes above 40°S was observed in 16 out of 21 cases and these high-latitude extensions would not be related to the ring shadow. A listing of the dropout events (Table S1) and a set of example cases of the dropouts in the low rate/survey spectrograms are provided in section S1 of the supporting information.

While the comparison of the high-frequency edge of the whistler mode signal to the LP has occurred at lower latitudes (like from 02:45 to 03:30 SCET in Figure 2; Wahlund et al., 2018), this comparison has not been made for the higher-latitude dropout features.

To confirm the dropout as being related to the electron density, we compared the dropout-derived electron density to the density obtained by the LP. At low densities below $\sim 5/\text{cm}^3$, the LP is influenced by local photoelectron emission, with the photoelectron currents to and from the probe representing a variable environmental noise floor (Hadid et al., 2018). There are two methods to obtain the low electron density values in the LP: (1) Values for n_e are obtained from high-resolution electron current measurements obtained when the probe is positively biased at +11.5 V and sampled at 20 samples per second (see Engelhardt et al.'s, 2015 section 2.1 and their Appendices A and C for a description of this 20-Hz sensing mode). This approach allows high sampling rates but is susceptible to modifications by the local photoelectron environment. (2) The floating potential, U_{float} , can be a proxy for electron density, as defined by equation (1) of Morooka et al. (2009), with $n_e \sim \exp(-AU_{\text{float}})$, where A is a constant. This proxy analysis is consistent with Cassini/CAPS-derived electron density values (see Figure 2 of Morooka et al., 2009). Overall, comparisons with the LP 20-Hz density include cases where the whistler mode dropout features nicely match an electron density dropout in the LP and others where the photoelectron emission alters or dominates the LP observations. Despite these effects, a change in the overall structure could be observed in the LP sweep summary plots (see a set of examples in section S4 of the supporting information) indicating a lower electron density and reduced electron energy distribution in direct association with the whistler mode high-frequency boundary dropout when connected to the A and B rings.

Figure 3 shows the LP electron density from its 20 Hz, proxy, and sweep measurement set along with the electron density inferred from the whistler mode high-frequency cutoff shown for the inbound case in Figure 2 near 02:40 SCET. We also include a wideband waveform spectrogram showing an intensified emission at the local electron plasma frequency, f_{pe} , displaying a frequency-decreasing tone between 02:38 and 02:39 SCET. The f_{pe} emission frequency decrease from ~ 8 to ~ 3 kHz during this time is consistent with the LP proxy observations of a decreasing electron density from 0.8 to $\sim 0.06/\text{cm}^3$ during this time.

As suggested in Figure 3, a second form of evidence of the connection of the dropout feature of the whistler mode high-frequency boundary to the electron density can be found in the high rate wideband waveform data, typically with individual spectra obtained at a rate of 125 ms (Gurnett et al., 2004). Given the fast sampling, additional evidence can be found in the form of an obvious emission at the local electron plasma frequency (f_{pe} emission) like in Figure 3 and/or a clear and distinct cutoff in the whistler mode boundary that acts to further confirm the low electron plasma frequency and electron densities in the regions. There were wideband data available in 30 of the 31 cases where a dropout was observed in the low rate data (like that in Figures 2 and 3). Of these, 25 out of 30 possessed a distinct f_{pe} emission or obvious cutoff feature at some point during the transit across ring-connected field lines further supporting the finding that the dropout is related to a decrease in electron density (a set of examples are found in section S3 of the supporting information). This connection thus presents added proof of existence of an electron plasma frequency/electron density dropout along A and B ring-connected field lines.

For each of the dropout cases identified in the low rate data (listed in Table S1), we cataloged the key features of the whistler mode dropout signatures, including the radial distance, the magnetic L shell value (Burton et al., 2010), and frequency of the inner edge of the dropout, the floor of the dropout, and the outer edge of the dropout. Throughout this work, we quote L shell values that, by definition, map to the radial distance at the magnetic equator. In the equatorial region out near $\sim 2 R_s$, the magnetic equator is shifted northward by about $0.04 R_s$ relative to the ring plane (Burton et al., 2010), and this shift maps to a small $< 0.002 R_s$ offset

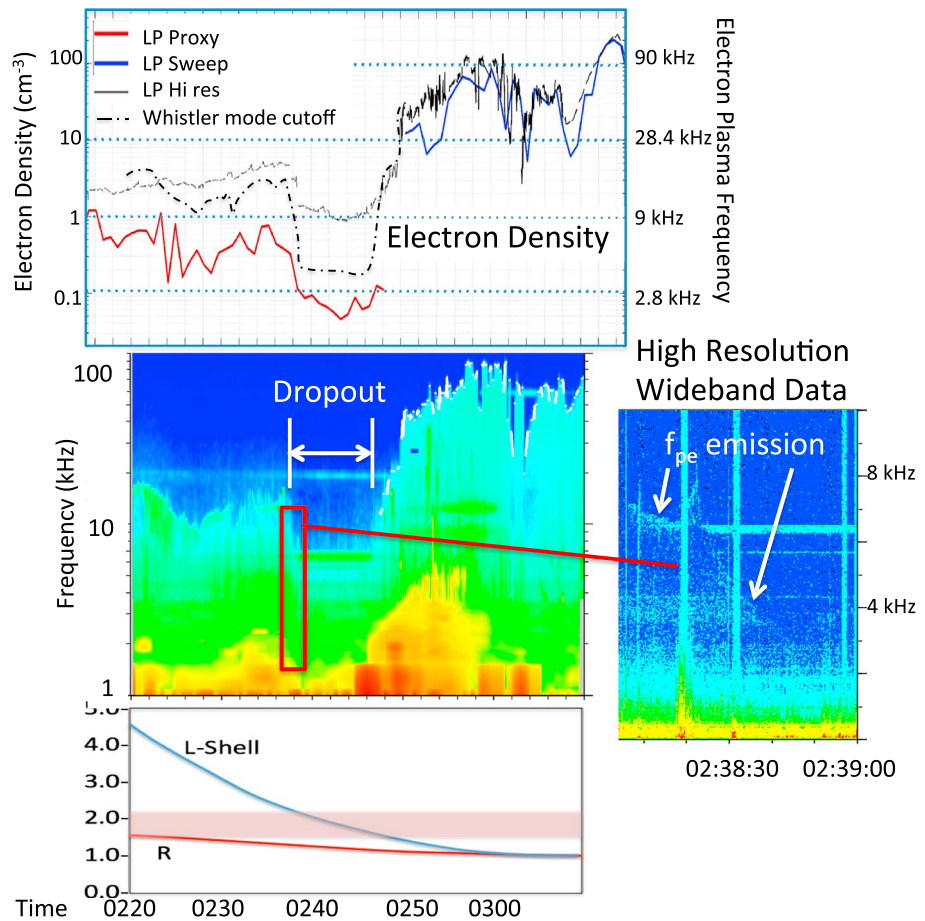


Figure 3. A comparison of the Langmuir probe electron density to the high-frequency boundary/cutoff of the whistler mode signal and high rate waveform data for the northern dropout on Rev 275 on 22 May 2017 (i.e., left half of Figure 2). There is a simultaneously measured dropout in the electron density and the low rate whistler mode cutoff. The whistler mode cutoff also identified the electron plasma frequency in the corresponding high rate data. All of this activity occurs at the outer edge of the dropout near $L \sim 2.27$. LP = Langmuir probe.

in the radial position of the magnetic field line in mapping from magnetic equator to ring plane. On the scale size of the variations in dropout features (see Figure 4), this is an insignificant shift.

3. Results

Figure 4 shows the Burton model L shell positions (Burton et al., 2010) of the inner edge, floor, and outer edge of the dropout features listed in Table S1. Given the evidence in the LP observation and wideband data, we infer that the whistler mode high-frequency dropout in the low rate observations is representative of a change in the electron plasma frequency during these times and thus, we converted the changes in the high-frequency boundary of the whistler mode emission to an electron density via $n_e = (f_{pe}/8,980)^2$ (Gurnett and Bhattacharjee (2005)). We then plot the electron density for those locations identified as the radially inner edge of the dropouts (represented by x), the density at the floor of the dropout features (represented by triangles), and the density at the transition back to nominal values (shown as squares) as a function of L shell. Figure 4a shows these dropout features versus L shell for the set of northern dropouts, and Figure 4 b shows the southern dropouts.

Figure 4 demonstrates that the presumptive electron density dropouts are consistently found between L shells of 1.5 to 2.3—overlying the A and B rings. They are found in both northern/Sun-illuminated and southern/Sun-shadowed regions. We find that the inner edge of the dropouts tend to occur over the C ring. The dropout features become apparent due to the superposed overlaying of the key features (inner edge,

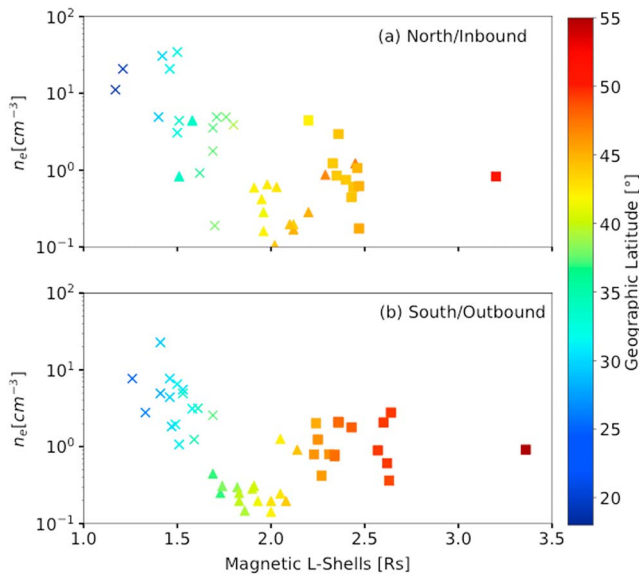


Figure 4. (a, b) The electron density derived from the set of whistler mode dropout events, as a function of the Burton magnetic field model L shell value (Burton et al., 2010). For each dropout event, we identified the frequency and spatial location of the dropout's inner edge, floor, and outer edge. These are listed in Table S1. We then plot these key dropout features with x indicative of the dropout's inner edge, triangle being the dropout floor, and square identifying the dropout's outer edge. Note that there is a consistent electron density dropout between the L shell of ~ 1.5 and 2.3 , on field lines connected to the main rings.

and B rings, the electrons at intermediate and small pitch angles might be lost on the quasi-solid surfaces and thus do not mirror from magnetic conjugate locations, thereby eliminating loss cone features. The elimination of the loss cone might then manifest itself as a change in whistler mode bandwidth, in association with the change in the nature of the instability features of the driving electron distribution.

However, the subsequent examination the wideband data for f_{pe} features revealed the dropouts to be indicative of decreases in the electron density over field lines connected to the rings (as evident in the f_{pe} emissions and resolved cutoff features shown in Figures S11 to S18). The LP observations also reinforce the explanation: These ring-connected field lines have depleted flux tubes compared to nonring-connected field lines.

4.2. Previous Predictions of Plasma Along Ring-Connected Flux Tubes

There are two very different views of the plasma content on ring-connected field lines. Given the observation of the spokes, which were thought to be impact generated, Wilson and Waite Jr. (1989) suggested that continual impacting onto the rings would create an enhanced warm plasma population, with flux peaking over the densest portion of the B ring where the meteoric impact incidence on solid material would be the greatest. The warm ring-originating plasma at densities of $3\text{--}30\text{ cm}^{-2}$ was thought to be created via impact ionization (see their plate 3). They then modeled the ambipolar expansion of cold electrons from the ionosphere and the added effect from this ring-originating warm electrons and heavy ions created by impacts, finding that the field lines connected to the B ring are dense containing both upward flowing ring and downward flowing ionospheric plasma.

In contrast, Tseng et al. (2010, 2013) modeled the formation of a more passive photolytic-driven ring ionosphere, and this model predicted the presence of plasma dropouts along the B ring (see Tseng et al., 2010, Figures 4a and 5, and Tseng et al., 2013, Figure 2b). They also find that the C ring emits ions that continually flow into the southern ionosphere due to an instability in the set of field-aligned forces identified previously by Northrup and Hill (1983). Our observations provide some validation to this model of a plasma density minimum along magnetic field lines connected to the B ring.

floor, and outer edge). The spread in these feature's L positions provides an approximate measure of the accuracy of position. While there is substantial spread, there is clear and obvious separation of the set of inner edge, floor, and outer edge L shell values. The dropout in plasma content over the A and B rings has values typically below $0.3/\text{cm}^3$ and represents about a factor of 5–10 density decrease compared to the plasma content at the outer edge of the dropout. We note that in Figure 4b, these features are influenced (contaminated in part) by the added effect of the shadows of the rings that creates a local decrease in electron content (Hadid et al., 2018). However, this ring shadow will not affect the dropouts observed above about 38°S . Thus, in Figure 4b, the transition from the floor to outer edge (i.e., the squares in the figure) is not in the ring shadow. For inbound/north passes, the dropouts were found between 1.28 and $1.33 R_s$, while during outbound/south passes the dropouts were detected at 1.2 and $1.3 R_s$ (see the discussion in section S2 of the supporting information for further analysis of the radial positioning of the set of dropouts).

4. Discussion and Conclusions

4.1. The Dropouts as Indicators of the f_{pe} Cutoffs

The dropouts in the high-frequency boundary of the whistler mode emission can have two possible explanations: (1) They are associated with a change in electron plasma frequency (or electron density), which limits the high-frequency extension of the whistler mode, and (2) an intrinsic change in the electron energy distribution on field lines connected to the rings, which in turn affects the whistler mode bandwidth and high-frequency extent. Specifically, for field lines connected to the main A

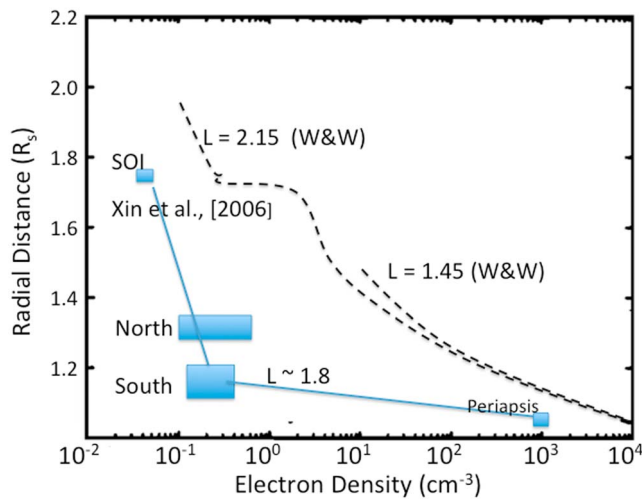


Figure 5. The profile of electron density as a function of radial distance along a field line connected to the central B ring. For comparison, we include the ambipolar model prediction from Wilson and Waite Jr. (1989) that includes the effect of a ring hot plasma source from impact ionization. Note that the observed electron densities are substantially lower than those predicted, in association with mostly evacuated flux tubes.

We note that Kaiser et al. (1984) reported on the possibility of electron density dropouts along ring-connected field lines using the atmospheric Saturn electrostatic discharges as a means to reveal the overlying electron density. They suggested therein the possibility that the main rings were a sink of plasma along connecting magnetic field lines.

4.3. Enhanced Ambipolar Diffusion

Figure 5 illustrates the densities measured by RPWS along field lines connected to the central B ring using the dropout density values from this study. Specifically, the range of dropout floor values in Figure 4 is placed in a set and labeled as *north* and *south* in the figure. We also include an initial low-altitude ionosphere density assuming that the electron density at $1.05 R_s$ is approximately 10^3 cm^{-3} , like that measured directly by the LP at periapsis at lower latitudes (Wahlund et al., 2018; labeled as *periapsis*). We also include the measured SOI minimum density from Xin et al. (2006) at $L \sim 1.76$ (labeled as *SOI*).

We find that Cassini is detecting electron densities between 1.1 and $1.3 R_s$ along $L \sim 1.5$ – 2.3 nearly 300 times lower than those densities predicted from the impact-driven ring ion outflow (at $10^7/\text{cm}^2\text{-s}$) of Wilson and Waite Jr. (1989). We include electron density profiles along ring-connected magnetic field lines from this model (identified in the figure as *W&W*).

Devoid of the warm impact plasma, the flux tubes over the A and B rings are relatively empty, thereby creating a strong ambipolar effect on the ionospheric plasma. These ambipolar E fields would get effectively *shorted out* if a large population of warm plasma was moving out of the rings and migrating upward and inward toward the ionosphere.

The ambipolar potential operating on the electrons along the $L \sim 1.8$ field line can be estimated assuming the density scales as $n_e \sim n_{eo} \exp(e\Phi/kT)$ (Wilson & Waite Jr., 1989). In this case, we apply a low altitude $n_{eo} \sim 10^3 \text{ cm}^{-3}$ and electron temperature $T \sim 0.086 \text{ eV}$ (1000 K) similar to the values $<4,000 \text{ km}$ shown in Figure 2 of Wahlund et al. (2018). While this direct observation was made near the equator, we assume that this density value is similar to that near 40° . The potential Φ is then $T \ln(n_e/n_{eo})$ with T in units of electron volts. From the ionosphere to the altitude of the proximal-detected depletions ($\sim 2,000 \text{ km}$), the ambipolar potential drop is about -0.7 V (i.e., a value of $n_e \sim 0.2 \text{ cm}^{-3}$ at $\sim 12,000 \text{ km}$ from Figure 5). There is another -0.14 V drop from these proximal-detected depletions to the deeper depletion detected during SOI. Assuming that ionospheric electrons fill the entire field line, there would be a total ambipolar potential drop of -0.84 V to account for the electron density profile. We note that this potential drop corresponds to the location over the shadowed ring surface. The Sun-facing surface likely has a population of photoelectrons that reduced the overall drop (Farrell et al., 2006).

4.4. Analog to the Terrestrial Plasmasphere Flux Tube Refilling Process

The evacuated field lines connected to the A and B rings are behaving analogously to evacuated flux tubes found in the terrestrial plasmasphere (Singh & Horwitz, 1992). Geomagnetically active periods in the terrestrial inner magnetosphere will create empty or depleted flux tubes in the terrestrial plasmasphere. Such flux tubes are subsequently filled in via strong ambipolar processes that draw electrons and ions out of the ionosphere to replenish/refill the tube. Much like Saturn's ring case presented herein, negative ambipolar potentials develop to draw out the ions and retard electron outflow. The plasma front driven by the ambipolar process then moves down field lines. In the terrestrial plasmasphere, plasma fronts from adjacent ionospheric footprints intersect in the equatorial region to create counterstreaming flows and possibly an electrostatic shock (Singh & Horwitz, 1992; Singh & Schunk, 1983; Singh et al., 2011). In the case of Saturn, the expanding plasma is lost on the solid surface rings, charging the rings.

In summary, there are clear and distinct decreases in the high-frequency boundary of the whistler mode emissions detected by the Cassini RPWS instrument at relatively high latitudes ($\pm 40^\circ$) during the proximal passes. These decreases or dropouts have start and stop locations that correspond to L shells at the edges

of the A and B rings and are indicative of a substantial reduction in electron density on these magnetic lines. The observations of evacuated flux tubes on ring-connected field lines are consistent with the presence of the ring plasma cavity feature observed over the A and B rings during the earlier SOI overflight. The unique set of ring-connected plasma measurements obtained in 2004 at the very beginning of the Cassini/Saturn observation period connects directly to the unique set of observations made 13 years later during the Grand Finale observation period.

Acknowledgments

The authors wish to thank NASA and the outstanding project team at JPL for contribution to mission success. We also thank the data processing team at the PI institution at Iowa for their constant high quality of work. All Cassini RPWS data are archived in the Planetary Data System (PDS) Planetary Plasma Interaction (PPI) node at <https://pds-ppi.igpp.ucla.edu/search/?t=Saturn&i=RPWS> on a prearranged schedule.

References

- Burton, M. E., Dougherty, M. K., & Russell, C. T. (2010). Saturn's internal planetary magnetic field. *Geophysical Research Letters*, 37, L24105. <https://doi.org/10.1029/2010GL045148>
- Connerney, J. E. P. (1986). Magnetic connection for Saturn's rings and atmosphere. *Geophysical Research Letters*, 13(8), 773–776. <https://doi.org/10.1029/GL013i008p00773>
- Connerney, J. E. P., & Waite, J. H. (1984). New model of Saturn's ionosphere with an influx of water from the rings. *Nature*, 312(5990), 136–138. <https://doi.org/10.1038/312136a0>
- Dougherty, M. K., Kellock, S., Southwood, D. J., Balogh, A., Smith, E. J., Tsurutani, B. T., et al. (2004). The Cassini magnetic field investigation. *Space Science Reviews*, 114(1–4), 331–383. <https://doi.org/10.1007/s11214-004-1432-2>
- Engelhardt, I. A. D., Wahalund, J.-E., Andrews, D. J., Eriksson, A. I., Ye, S., Kurth, W. S., et al. (2015). Plasma regions, charged dust and field aligned currents near Enceladus. *Planetary and Space Science*, 117, 453–469. <https://doi.org/10.1016/j.pss.2015.09.010>
- Farrell, W. M., Desch, M. D., Kaiser, M. L., Kurth, W. S., & Gurnett, D. A. (2006). Changing electrical nature of Saturn's rings: Implications for spoke formation. *Geophysical Research Letters*, 33, L07203. <https://doi.org/10.1029/2005GL024922>
- Farrell, W. M., Kurth, W. S., Gurnett, D. A., Persoon, A. M., & MacDowall, R. J. (2017). Saturn's rings and associated ring plasma cavity: Evidence for slow ring erosion. *Icarus*, 292, 48–53. <https://doi.org/10.1016/j.icarus.2017.03.022>
- Gurnett, D. A., & Bhattacharjee, A. (2005). *Introduction to plasma physics with space and laboratory applications*. Cambridge, UK: University Press. <https://doi.org/10.1017/CBO9780511809125>
- Gurnett, D. A., Kurth, W. S., Kirchner, D. L., Hospodarsky, G. B., Averkamp, T. F., Zarka, P., et al. (2004). The Cassini radio and plasma wave investigation. *Space Science Reviews*, 114(1–4), 395–463. <https://doi.org/10.1007/s11214-004-1434-0>
- Gurnett, D. A., Kurth, W. S., Hospodarsky, G. B., Persoon, A. M., Averkamp, T. F., Cecconi, B., et al. (2005). Radio and plasma wave observations at Saturn from Cassini's approach and first orbit. *Science*, 307(5713), 1255–1259. <https://doi.org/10.1126/science.1105356>
- Hadid, L. Z. M., Morooka, W., Wahlund, J.-E., Moore, L., Cravens, T. E., Hedman, M. M., et al. (2018). Ring shadowing effects on Saturn's ionosphere: Implications for ring opacity and plasma transport. *Geophysical Research Letters*. <https://doi.org/10.1029/2018GL079150>
- Kaiser, M. L., Desch, M. D., & Connerney, J. E. P. (1984). Saturn's ionosphere—Inferred electron densities. *Journal of Geophysical Research*, 89(A4), 2371–2376. <https://doi.org/10.1029/JA089iA04p02371>
- Menietti, J. D., Averkamp, T. V., Ye, S.-Y., Sulaiman, A., Morooka, M., Persoon, A. M., et al. (2018). Analysis of intense Z-mode emission observed during the Cassini proximal orbits. *Geophysical Research Letters*. <https://doi.org/10.1002/2018GL077354>, in press
- Morooka, M. W., Modolo, R., Wahlund, J.-E., André, M., Eriksson, A. I., Persoon, A. M., et al. (2009). The electron density of Saturn's magnetosphere. *Annales Geophysicae*, 27, 2971–2991.
- Northrup, T. G., & Hill, J. R. (1983). The inner edge of Saturn's B ring. *Journal of Geophysical Research*, 88(A8), 6102–6108. <https://doi.org/10.1029/JA088iA08p06102>
- Persoon, A. M., Gurnett, D. A., Kurth, W. S., Groene, J. B., & Faden, J. B. (2015). Evidence for a seasonally dependent ring plasma in the region between Saturn's A ring and Enceladus' orbit. *Journal of Geophysical Research: Space Physics*, 120, 6276–6285. <https://doi.org/10.1002/2015JA021180>
- Singh, A. H., Singh, R. P., & Siingh, D. (2011). State studies of Earth's plasmasphere. *Planetary and Space Science*, 59(9), 810–834. <https://doi.org/10.1016/j.pss.2011.03.013>
- Singh, N., & Horwitz, J. L. (1992). Plasmasphere refilling: Recent observations and modeling. *Journal of Geophysical Research*, 97(A2), 1049–1079. <https://doi.org/10.1029/91JA02602>
- Singh, N., & Schunk, R. W. (1983). Numerical simulations of counterstreaming plasmas and their relevance to interhemispheric flows. *Journal of Geophysical Research*, 88(A10), 7867–7877. <https://doi.org/10.1029/JA088iA10p07867>
- Tseng, W.-L., Ip, W. H., Johnson, R. E., Cassidy, T. A., & Elrod, M. K. (2010). The structure and time variability of the ring atmosphere and ionosphere. *Icarus*, 206(2), 382–389. <https://doi.org/10.1016/j.icarus.2009.05.019>
- Tseng, W.-L., Johnson, R. E., & Elrod, M. K. (2013). Modeling the seasonal variability of the plasma environment in Saturn's magnetosphere between main rings and Mimas. *Planetary and Space Science*, 77, 126–135. <https://doi.org/10.1016/j.pss.2012.05.001>
- Wahlund, J.-E., Morooka, M. W., Hadid, L. Z., Persoon, A. M., Farrell, W. M., Gurnett, D. A., et al. (2018). In situ measurements of Saturn's ionosphere show it is dynamic and interacts with the rings. *Science*, 359(6371), 66–68. <https://doi.org/10.1126/science.aao4134>
- Wilson, G. R., & Waite, J. H. Jr. (1989). Kinetic modeling of the Saturn ring-ionosphere plasma environment. *Journal of Geophysical Research*, 94(A12), 17,287–17,298. <https://doi.org/10.1029/JA094iA12p17287>
- Xin, L., Gurnett, D. A., Santolik, O., Kurth, W. S., & Hospodarsky, G. B. (2006). Whistler-mode auroral hiss emissions observed near Saturn's B ring. *Journal of Geophysical Research*, 111, A06214. <https://doi.org/10.1029/2005JA011432>
- Young, D. T., Berthelier, J. J., Blanc, M., Burch, J. L., Bolton, S., Coates, A. J., et al. (2005). Composition and dynamics of plasma in Saturn's magnetosphere. *Science*, 307(5713), 1262–1266. <https://doi.org/10.1126/science.1106151>